Supplement of Atmos. Chem. Phys., 17, 11779–11801, 2017
https://doi.org/10.5194/acp-17-11779-2017-supplement

Supplement of

CCN activity and organic hygroscopicity of aerosols downwind of an urban region in central Amazonia: seasonal and diel variations and impact of anthropogenic emissions

Ryan Thalman et al.

Correspondence to: Jian Wang (jian@bnl.gov)

1 Calibration and Operation of the CCN counter

The system used to measure size-resolved CCN spectra during GoAmazon 2014/5 is shown in Fig. S1, and the operation sequences of DMA classified particle diameter, Q_{CCN} and ΔT are present in Fig. S2. The CCN counter was calibrated at each flow and temperature setting using ammonium sulfate as an inorganic aerosol standard (Lance et al., 2006; Mei et al., 2013; Roberts and Nenes, 2005; Shilling et al., 2007). As the temperatures at the top of the CCN counter column (T_1) varies with room temperature, the calibration was repeated for each pair of Q_{CCN} and ΔT over a range of T_1 typically encountered during GoAmazon 2014/5. The calibration results are shown as a function of Q_{CCN} and ΔT conditions at T_1 = 25°C in Fig. S3, and the variation of instrument supersaturation (SS) with respect to T_1 is present in Fig. S4. Instrument supersaturation during the measurements was calculated using the Q_{CCN}, ΔT, and T_1 based on the calibrations.

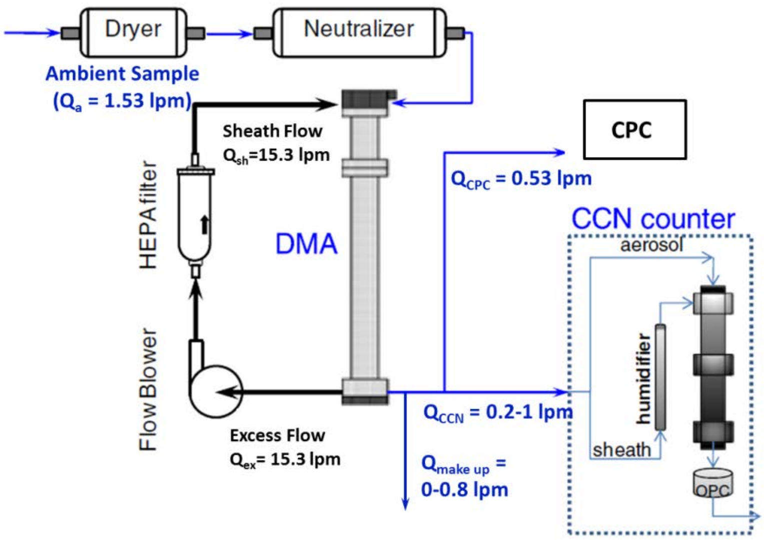

Figure S1: Schematic of the system for measuring size-resolved CCN spectra during GoAmazon 2014/5.

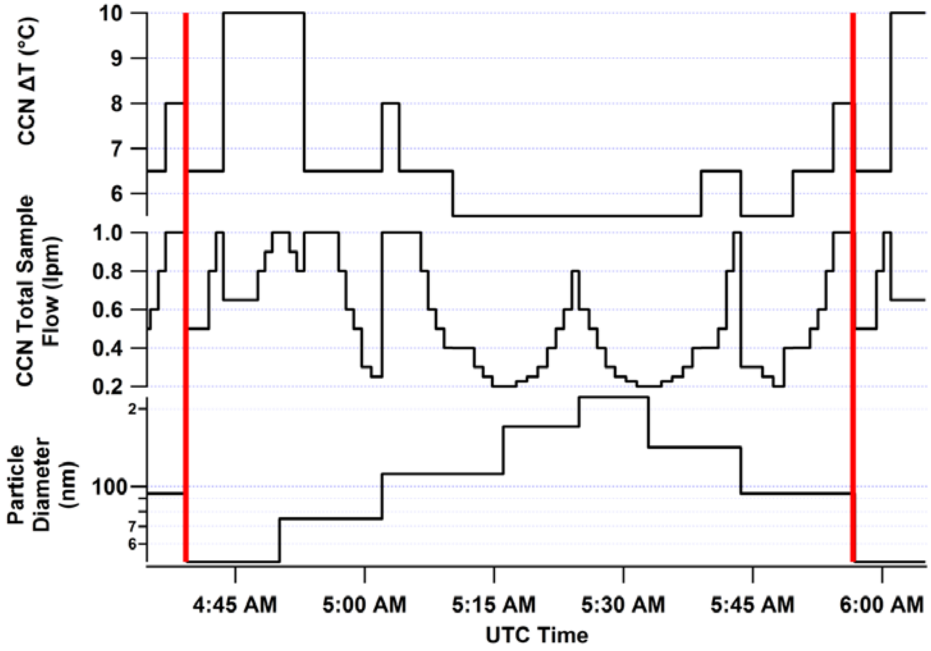

Figure S2: Instrument operation sequence showing set points of DMA classified particle diameter, Q_{CCN} and ΔT for one full measurement cycle. Red vertical lines mark the start and finish of one cycle.

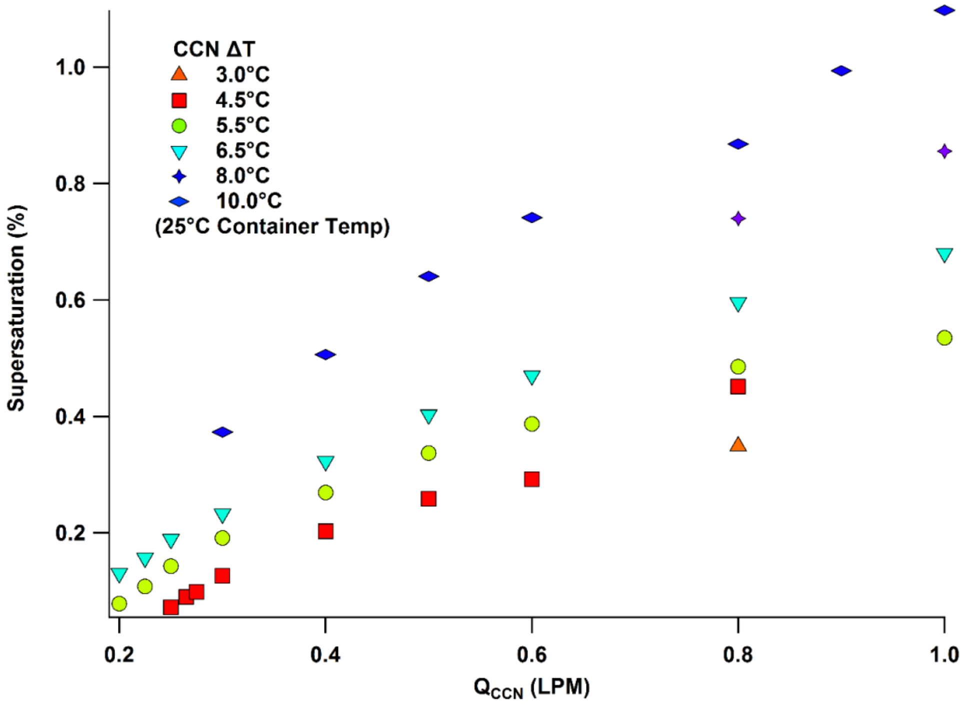

Figure S3: Calibrated CCN counter supersaturation as a function of ΔT at T_1 of 25°C for Q_{CCN} ranging from 0.2 to 1.0 LPM.

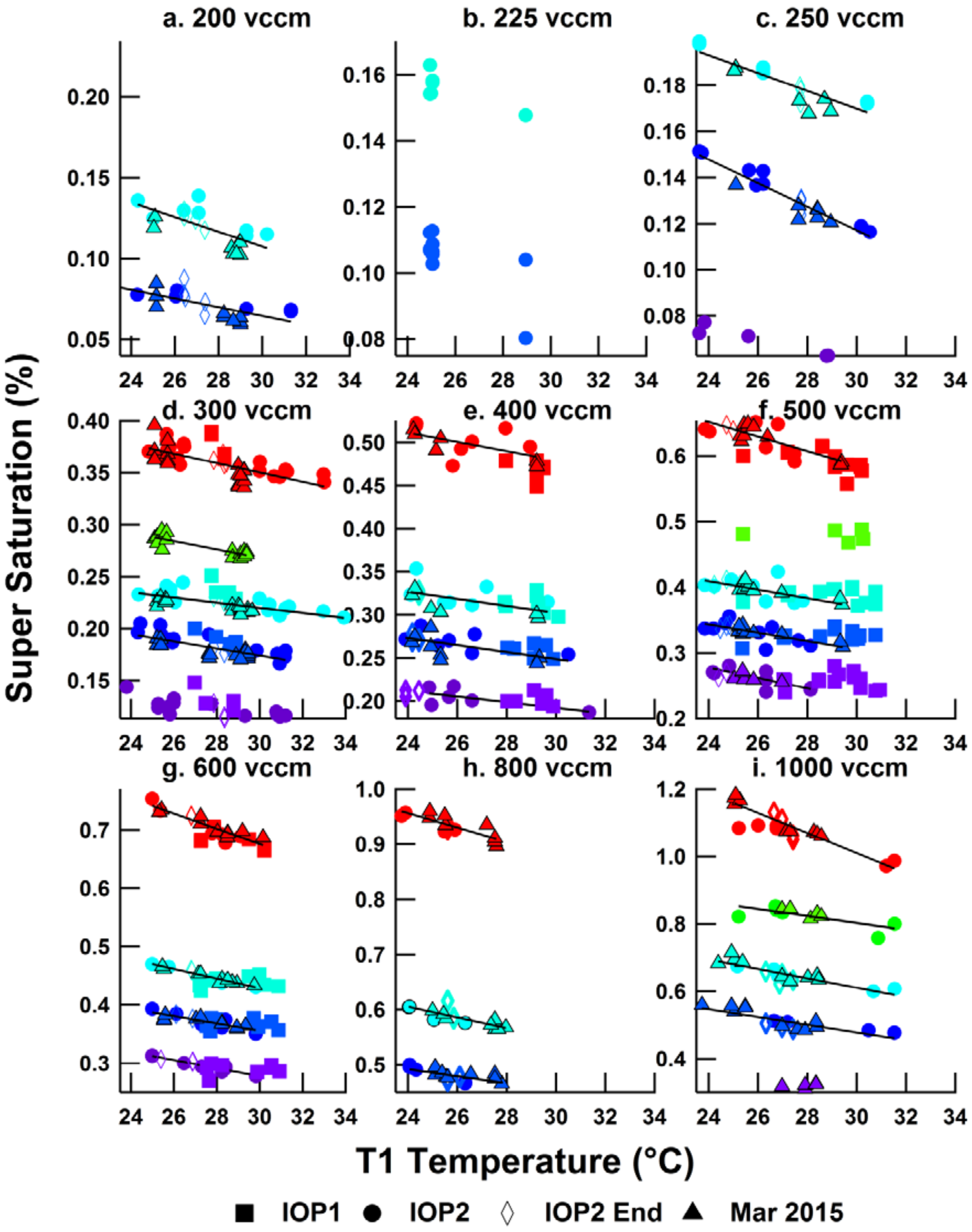

Figure S4: Calibrated instrument supersaturation as a function of T_1 for different ΔT and Q_{CCN} values. The symbol colors of purple, dark blue, light blue, green and red correspond to ΔT values of 4.5, 5.5, 6.5, 8.0, and 10.0°C, respectively. Calibrations were carried out throughout the entire campaign (February/March 2014 - ■; August 2014 - ●; October 2014 - ◊; March 2015 - ▲). The lines represent least square fits of the calibration results.

2 ARM Facility Instruments

2.1 Measurements of Oxides of Nitrogen

Oxides of nitrogen were measured by catalytic conversion to NO and chemiluminescence at one minute time resolution. The $NO/NO_2/NO_y$ system is based on two Thermo Scientific 43i instruments and customized by Air Quality Design, Inc. (Wheatridge, CO) for detection of NO. The inlet/converter box is external and located at 10 meters above ground level and is environmentally controlled. A dedicated channel converts total NOy ($NO + NO_2 + HNO_3$ + peroxy acyl nitrates + aerosol nitrates, but not NH_4) to NO via a Mo catalyst heated to 325°C. A second channel converts NO_2 to NO by a light emitting diode (LED) photolysis cell with 50% conversion efficiency (C.E.). The LED is toggled on and off on a two minute cycle to measure ambient NO and NO + C.E.× NO_2, and the NO_2 mixing ratio is derived from the difference of the measurements. The inlet box contains mass flow controllers (MFCs) so that the residence time to the chemiluminescence cells is minimal and occurs at reduced pressure. The unit is calibrated daily with standard additions of NO and NO_2 to measure the conversion efficiency of both the Mo converter (1.00±0.02) and the photolysis cell.

2.2 Refractory Black Carbon Measurements

The incandescence signal measured by SP2 is proportional to the mass of rBC in the particles irrespective of whether the rBC is coated or not (Moteki et al., 2007; Schwarz et al., 2010; Stephens et al., 2003). The SP2 was calibrated using size-selected fullerene soot with no corrections for non-rBC content. The detectable size range of the SP2 is 75 – 600 nm (volume equivalent diameter), which typically provides a direct measurement of > 90% of rBC mass concentrations. If necessary, the complete mass size distribution is extrapolated to include rBC outside of this size range assuming a log-normal distribution (Mei et al., 2013). During

GoAmazon 2014/5, rBC mass was mostly within the detectable range. In contrast to the SP2, the seven-wavelength Aethalometer (Arnott et al., 2005; Hansen et al., 1984) reports an equivalent black carbon mass loading by converting a light absorption measurement from aerosols accumulated on a filter relative to a manufacturer-supplied conversion. However, there is substantial and growing evidence relating to measurement artifacts attributed to aerosol loading effects and enhanced light absorption through multiple-scattering of photons (Collaud Coen et al., 2010; Rizzo et al., 2011; Schmid et al., 2006; Virkkula et al., 2015; Virkkula et al., 2007; Weingartner et al., 2003). Given the more complete dataset of the Aethalometer, our analysis utilized the Aethalometer data only when SP2 data was unavailable. The available concurrent SP2 and Aethalometer datasets were used to derive a linear relationship to correct for Aethalometer measurement artifacts cited above. The mass concentrations of refractory black carbon (rBC) derived from SP2 and Aethalometer data were averaged to a common time base and the least square linear fit between both rBC mass concentrations is shown in Fig. S5 for both the wet and dry seasons. The linear relationship exhibited a seasonal dependence, which might be driven by variations in RH, the ratio of mass concentrations of organics to BC, or a combination of both. The rBC mass concentration derived from the Aethalometer measurement was used to fill the gaps in the SP2 data after scaled using the linear relationship corresponding to the respective season.

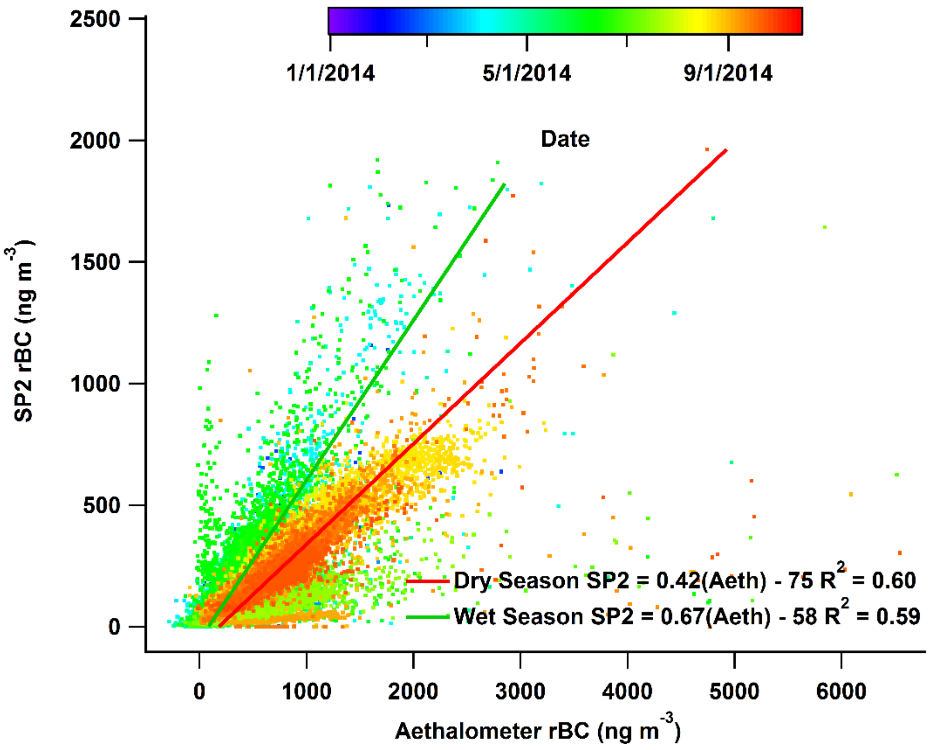

Figure S5: Correlation between rBC mass concentrations derived from the Aethalometer and SP2 measurements. Data points are colored by the time of the measurements. The red and green lines represent least square fit of data collected during the dry and wet seasons, respectively.

3 Reduction of the size resolved CCN activation spectrum

3.1 Correction for multiple charging

Size-resolved CCN activation fraction was characterized at particle diameters of 51, 75, 94, 112, 142, 171 and 222 nm. These sampling sizes were selected to form a progression of particle diameters corresponding to doubly and triply charged particles (e.g. 112 nm corresponds to the diameter of doubly charged particles, when the DMA is set to select particles with a diameter of 75 nm. See Table S1 for more details). The contribution of doubly and triply charged particles to the activation fraction was corrected using the size distribution measured by the SMPS (Model 3080 TSI, Inc) in MAOS and particle charging probabilities (Wiedensohler, 1988). In cases when the size distribution data were not available, we used the concentrations of classified particles measured by the CPC in the size-resolved CCN system when sampling at corresponding multiple-charged sizes. The impact of multiple-charged particles on activation fraction was then accounted for using the concentration of multiple-charged particles and the measured activation fractions at the corresponding sizes. This is similar to the methods established in the literature (Rose et al., 2008). When direct measurements of the activation fraction of multiple charged particles were not available, the multiple charged particles were assumed to have the same distribution of κ as the singly charge particles, and the activation fraction was corrected using the following iterative approach. First, the activation fractions of multiple charged particles were derived from the measured activation factions, taken into consideration the same κ distribution but larger particle diameters. These derived activation fractions at multiple charged sizes were then used to correct measured activation fraction using the approach described above. This process was continued until the corrected activation fraction of singly charged particles converged.

3.2 Data quality control criteria

Several quality-control criteria were applied to the data and results from the fitting of activation spectrum. The measurement of the entire activation spectrum at a single particle diameter took about 5-20 minutes. Individual points (i.e., activation fraction at a single S) of an activation spectrum were excluded from the fitting if the standard deviation of 1-sec measurements of the classified particle concentration is greater than 30% of the mean value for the current size, or single data points are more than 1.5 times the mean. This is to remove large fluctuation or spikes in CPC concentration due to contamination by emission of site generator or traffic. The removal of measurement at single supersaturation typically does not prevent fitting of the activation spectrum using data at remaining supersaturation points. Parameters derived from the fitting of activation spectrum were flagged and excluded from further analysis in this study for the following scenarios:

1. The fitted S^* is outside the supersaturation range of the measured activation spectrum.
2. The fitted maximum activated fraction (E) is not within 15% of any activated fraction measured at the three highest supersaturations. This indicates that the activation fraction did not reach a plateau even at the highest supersaturations sampled, and therefore E is not well constrained by the activation spectrum.
3. The residue of the fit is greater than 0.1. This indicates relatively poor fit, which represented less 1% of the activation spectra.
4. The fitted E is less than 0.5, indicating external mixtures with substantial fraction of fresh black carbon and primary organic aerosols emitted by the generator, vehicles, and grass cutting activities at or near the site.

For the one-year measurement period, 6.5 % of the total activation curves were removed by the above data quality filters.

3.4 Deriving average particle hygroscopicity and hygroscopicity dispersion from activation spectrum

For particles with the same size and composition (i.e., hygroscopicity), a step increase of R_a from 0% to 100% with increasing supersaturation is expected because all particles would have the identical critical supersaturation (S_c). The measurements of ambient aerosols show more gradual increase in R_a (i.e., instead of a step change), suggesting heterogeneity in particle S_c. The heterogeneity in particle S_c, as described by σ_s is due to a combination of width of DMA transfer function (particles classified by a DMA do not have exactly the same size), instrument non-idealities, and the heterogeneity in particle hygroscopicity. The value of σ_s due to the heterogeneity in particle hygroscopicity alone can be estimated by:

$$\sigma_s = \sqrt{\sigma_{s,\mathrm{m}}^2 - \sigma_{s,\mathrm{AS}}^2} \tag{S1}$$

Where $\sigma_{s,\mathrm{m}}$ and $\sigma_{s,\mathrm{AS}}$ are the values corresponding to the ambient measurement and the calibration using ammonium sulfate, respectively (Supplementary Information, Mei et al., 2013). Particle critical supersaturation S_c is related to hygroscopicity κ by (Petters and Kreidenweis, 2007):

$$\begin{aligned} S_\mathrm{c}\left(\kappa\right) &= \left(\frac{4A^3}{27D_\mathrm{p}^3\kappa}\right)^{1/2}, \\ A &= \frac{4\sigma_\mathrm{w}M_\mathrm{w}}{RT\rho_\mathrm{w}} \end{aligned} \tag{S2}$$

Where D_p is the particle diameter, M_w, ρ_w and σ_w are the molecular weight, density and surface tension of water, respectively. The probability distribution function of particle hygroscopicity $p\left(\kappa\right)$ can be derived as the following:

$$p\left(\kappa\right) = -\frac{dR_\mathrm{a}\left(S_\mathrm{c}\left(\kappa\right)\right)}{d\kappa} \tag{S3}$$

Where R_a is the fitted active spectrum with σ_s adjusted using Eq. (S1). We note that Eq. (S2) represents an approximation (Petters and Kreidenweis, 2007). For this study, the uncertainty of derived κ values due to this approximation is negligible. The dispersion of κ, which describes the heterogeneity of hygroscopicity for activated particles, is given by (Mei et al., 2013):

$$\sigma\left(\kappa\right)/\overline{\kappa_\mathrm{CCN}} = \left[\exp\left(4\sigma_s^2\right)-1\right]^{1/2} \tag{S4}$$

where $\sigma(\kappa)$ and $\overline{\kappa_{\mathrm{CCN}}}$ are the standard deviation and average value of the hygroscopicity for activated particles.

It is worth noting that because of the skewness of the lognormal distribution, the average particle hygroscopicity $\overline{\kappa_{\mathrm{CCN}}}$ is higher than κ^*, which corresponds to the fitted S^*, and represents the median hygroscopicity of activated particles (Fig. S6). The difference between $\overline{\kappa_{\mathrm{CCN}}}$ and κ^* becomes significant at high σ_s values (Fig. S7). In this study, $\overline{\kappa_{\mathrm{CCN}}}$ is derived from the probability density function using the following equation:

$$\overline{\kappa_{\mathrm{CCN}}} = \frac{\int_0^{0.65} \kappa \cdot p(\kappa)\, d\kappa}{\int_0^{0.65} p(\kappa)\, d\kappa} \qquad \text{(S5)}$$

The upper limit of the integration is limited to 0.65, which reflects the maximum particle hygroscopicity expected at the T3 site. The organic hygroscopicity is derived from the average particle hygroscopicity $\overline{\kappa_{\mathrm{CCN}}}$ and average chemical composition.

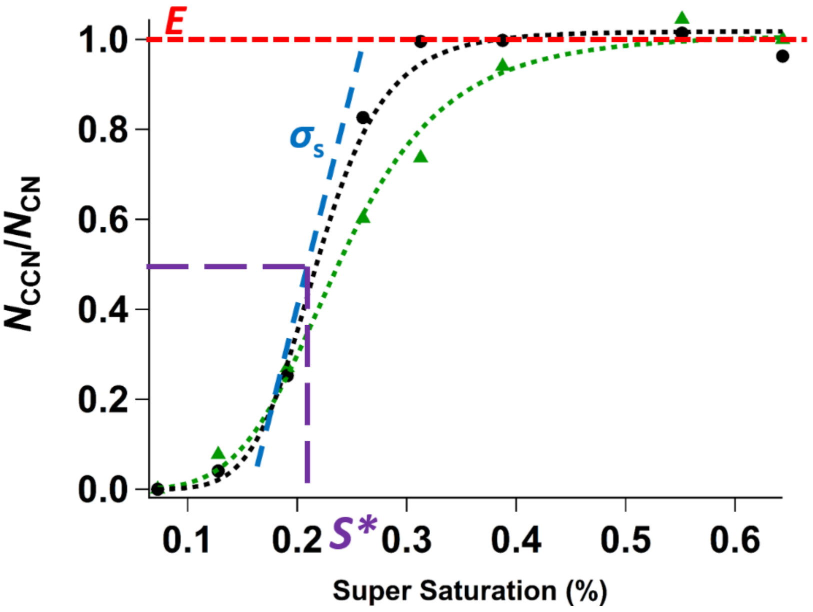

Figure S6: Sample activation spectra for particles with diameter of 142 nm. The black dots and green triangles represent spectra with a low dispersion (σ_s = 0.2; $\sigma(\kappa)/\overline{\kappa_{\mathrm{CCN}}} = 0.4$) and a much higher dispersion (σ_s = 0.4; $\sigma(\kappa)/\overline{\kappa_{\mathrm{CCN}}} = 0.9$), respectively.

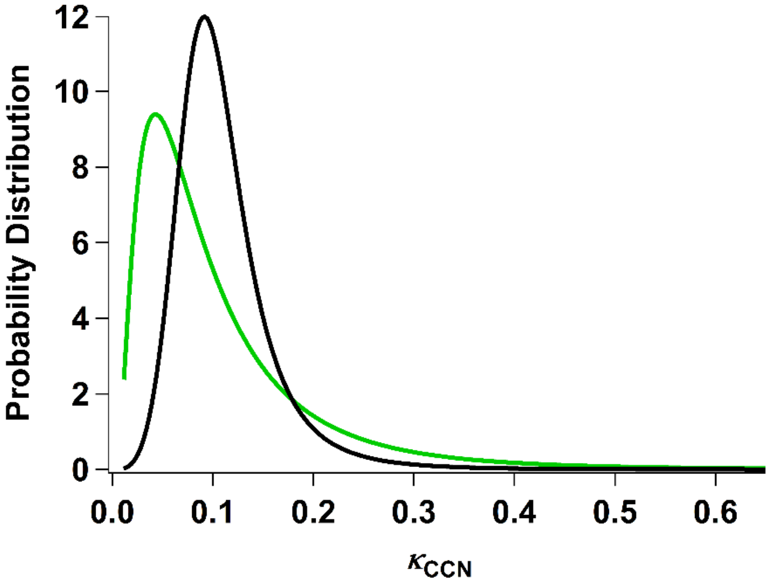

Figure S7: Probability density distributions of particle hygroscopicity derived from the fitted activation spectra shown in Figure S6. As dispersion increases, the distribution becomes increasingly asymmetric, and the difference between $\overline{\kappa_{\mathrm{CCN}}}$ and κ* increases.

4 Aerosol composition derived from AMS and rBC measurements

4.1 Bulk and size-resolved mass concentration of aerosol species

Given the very low aerosol mass concentration in the Amazon basin, the signal to noise ratio of particle time-of-flight (P-ToF) mode measurement was not sufficient to directly provide size resolved species mass concentrations for individual CCN activation spectrum. Instead, the size resolved species mass concentrations were constructed by combing the bulk mass concentrations measured in MS mode, which have higher signal to noise ratio, and P-ToF mode size resolved species mass distributions averaged over extended time periods. For both IOPs, the bulk organics mass fraction was derived from MS mode portion of individual AMS measurement. Based on the bulk organic mass fraction, measurements during IOP1 were then classified into three groups with equal number of measurements, and the characteristic mass size distribution of each species (i.e., organics, SO_4, NO_3, and NH_4) was averaged from P-ToF measurements within each group. For IOP2, the measurements were classified into three groups each for day and night periods based on the bulk aerosol organic mass fraction, and the mass size distribution of each species was averaged from P-ToF measurements in each of the six groups. The average mass size distributions of the four species for the three groups during the daytime of IOP2 are shown in Fig. S8 as examples. The underlying assumption is that observed aerosols exhibiting similar bulk composition (i.e., organic mass fraction) during the IOPs also had species mass size distributions with the same shapes. The vacuum aerodynamic diameter (D_{va}) measured by the AMS was converted to particle mobility diameter (D_m) and volume equivalent diameter (D_v) using the particle density with the assumption of spherical particles, which is reasonable given most of the aerosol observed at T3 site were quite aged. The average densities were calculated using the approach described in Kuwata et al. (2012), and were 1.45 $\mu g\ m^3$ and 1.47 during IOP 1 and 2, respectively. In this study, unless otherwise indicated, particle diameter D_p represents the mobility diameter (D_m), which is equivalent to the volume average diameter given the assumption of spherical particles.

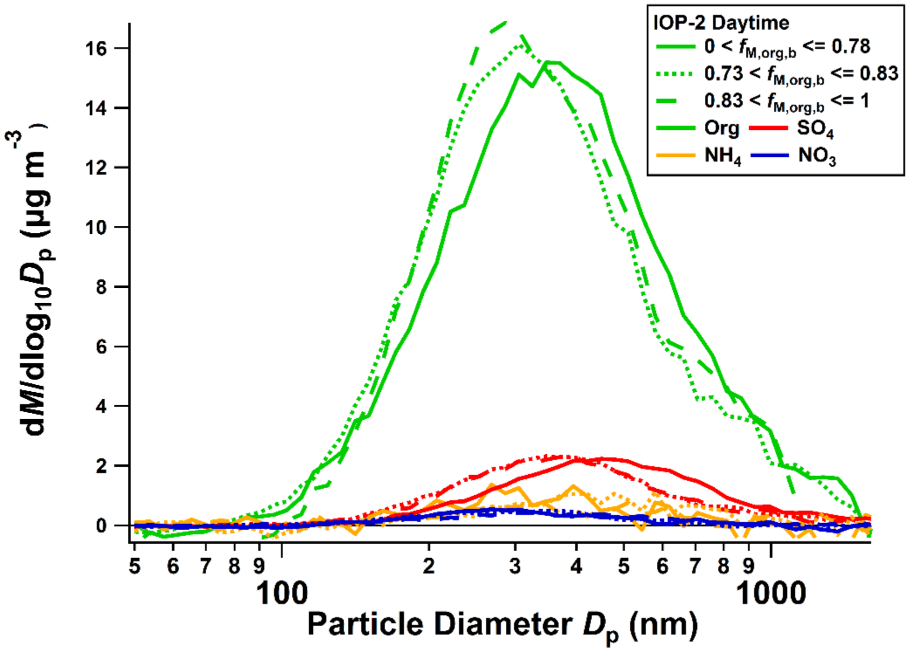

Figure S8: Size resolved mass concentrations of organics, SO_4, NO_3, and NH_4 averaged from P-ToF measurements for each of three groups during the day time of IOP2 (dry season). The three groups were classified based on bulk organics mass fraction ($f_{M,org}$).

For individual AMS measurements, the size resolve chemical composition was then derived as follows: the organic mass concentration at the particle diameter of CCN measurements, $m_{org}\left(D_p\right)$, was calculated as:

$$m_{org}\left(D_p\right)=M_{org,b}\times\frac{\overline{m}_{org}\left(D_p\right)}{\int_{D_{p,\min}}^{D_{p,\max}}\overline{m}_{org}\left(D_p^{'}\right)d\log D_p^{'}} \qquad \text{(S6)}$$

where $M_{org,b}$ is the bulk organic mass concentration from MS mode measurement, $\overline{m}_{org}(D_p)$ is the average organic mass size distribution with respect to $\log D_p$, $D_{p,\max}$ and $D_{p,\min}$ are the maximum and minimum diameters of the average mass size distribution. Using the same approach, the mass concentration of $\mathrm{SO_4^{2-}}$, $\mathrm{NO_3^-}$, and $\mathrm{NH_4^+}$ at specific D_p are calculated using the corresponding average mass size distributions. Mass concentration for black carbon $m_{rBC}(D_\mathrm{p})$ is derived with the assumption that the mass size distribution of rBC has the same shape of the total mass size distribution:

$$f_{M,rBC} = \frac{M_{rBC,b}}{M_{total,b}} = \frac{m_{rBC}(D_p)}{m_{\mathrm{SO_4^{2-}}}\left(D_p\right) + m_{\mathrm{NO_3^-}}\left(D_p\right) + m_{\mathrm{NH_4^+}}\left(D_p\right) + m_{org}(D_p) + m_{rBC}(D_p)} \qquad \text{(S7)}$$

where $f_{M,rBC}$ is the bulk mass fraction of refractory black carbon, $M_{rBC,b}$ and $M_{total,b}$ are the bulk rBC and total aerosol mass concentrations, respectively. From Eq. (S7), $m_{rBC}(D_p)$ can be derived as:

$$m_{rBC}\left(D_p\right) = \frac{f_{M,rBC}\left[m_{\mathrm{SO_4^{2-}}}\left(D_p\right) + m_{\mathrm{NO_3^-}}\left(D_p\right) + m_{\mathrm{NH_4^+}}\left(D_p\right) + m_{org}\left(D_p\right)\right]}{\left(1 - f_{M,rBC}\right)} \qquad \text{(S8)}$$

The fractional chemical composition at the size of CCN measurement D_p was then derived from the species mass concentrations calculated above. While not perfect, this approach allowed us to take both the temporal variation and size dependence of species mass concentrations into consideration when deriving particle composition at the sizes of CCN measurements. This is important because the organic volume fraction, required to derive the organic hygroscopicity was often much higher at the sizes of CCN measurements than that based on the bulk measurements.

4.2 Sulfate and nitrate

Outside of the IOP periods, particle composition was derived from ACSM data, and the retrieval of organonitrate mass concentration is not available. In addition, the detection limit of $\mathrm{NH_4^+}$ for the ACSM is very high, such that the measurement of $\mathrm{NH_4^+}$ mass concentration was too noisy for determining aerosol ionic balance. The sensitivity of derived κ_{org} to the assumption on nitrate was examined using the AMS data from the two IOPs to inform the appropriate assumptions for the analysis outside the IOP periods. Organic hygroscopicity was calculated using three different approaches: (1) the approach based on the retrievals of both inorganic and organic nitrate mass concentrations from AMS, as described in section 3.2 of the main text, (2) all $\mathrm{NO_3^-}$ was assumed from NH_4NO_3 and all sulfate from ammonium sulfate, and (3) all $\mathrm{NO_3^-}$ was from organonitrate with all sulfate from ammonium sulfate. κ_{org} derived using the three different assumptions are shown in Figure S9 for both IOPs. When all $\mathrm{NO_3^-}$ is assumed from organonitrate (i.e., approach 3), the derived κ_{org} values are very close to those based on retrieved organonitrate and inorganic nitrate concentrations from AMS data (i.e., approach 1). As a result, for measurements outside of the two IOPs when only ACSM measurements are available, all measured $\mathrm{NO_3^-}$ was assumed from organonitrate and sulfate was assumed from ammonium sulfate.

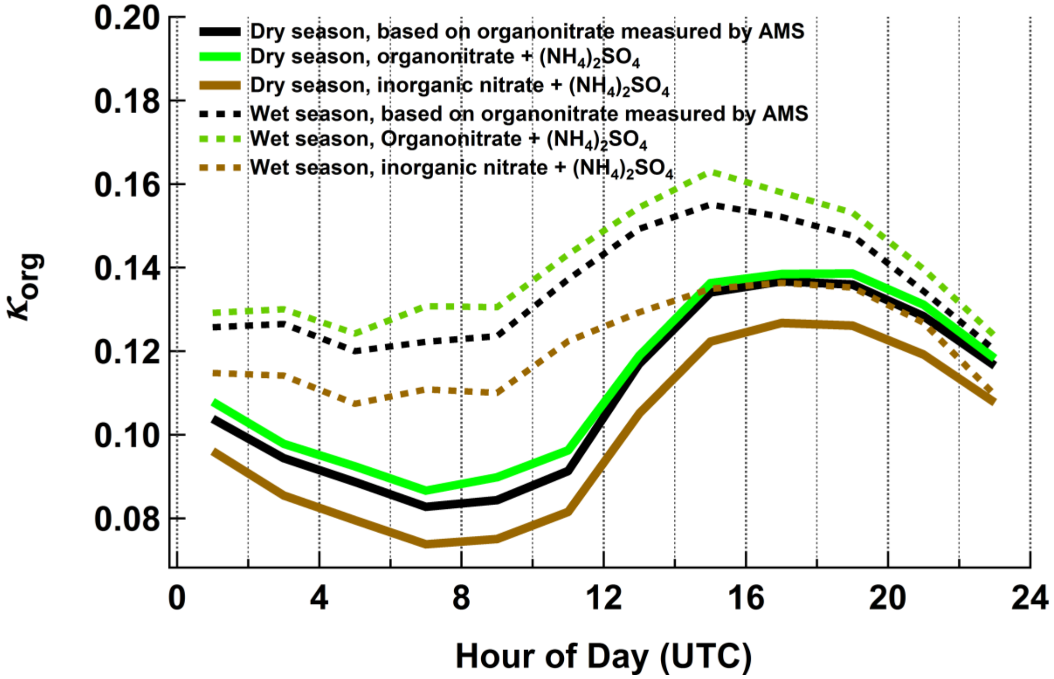

Figure S9: Diel variations of organic hygroscopicity derived using the three different assumptions on nitrate described in the text (i.e., mixed inorganic/organic nitrates, all organic nitrate, and all inorganic nitrate).

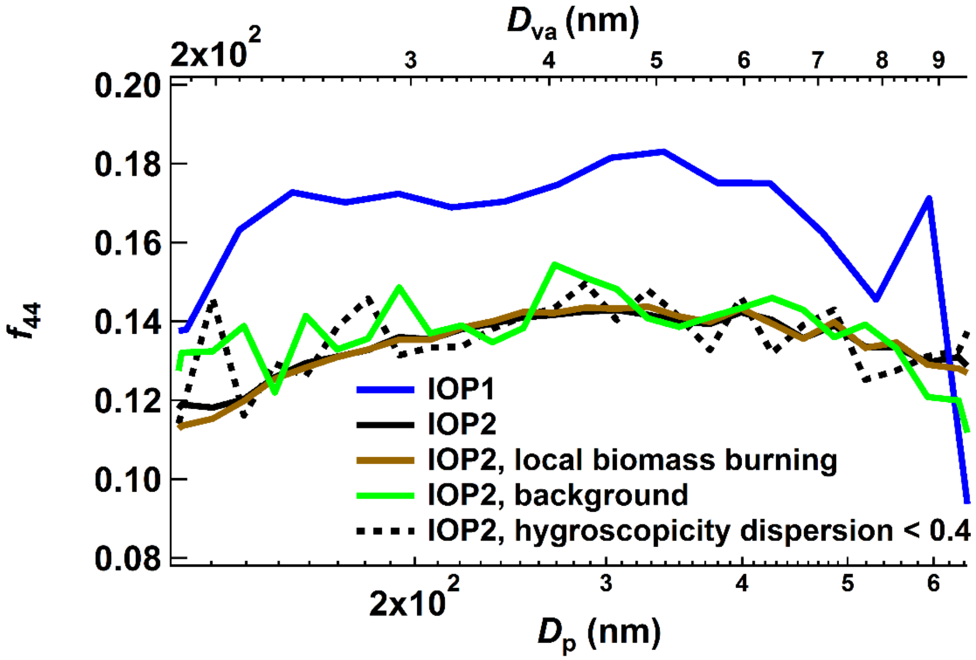

Figure S10: Size dependence of the fraction of the organic mass at m/z = 44 (f_{44}), which is indicative of the extent of oxidation. The f_{44} averaged during IOP1 was essentially independent of particle diameter D_p from 140 to 400 nm, a size range that dominated bulk organic mass concentration and encompasses the diameters of CCN measurements (i.e., 142 and 171 nm). During the IOP2, f_{44} averaged for all data and local biomass burning air mass type showed a clear dependence on D_p. In comparison, f_{44} averaged for the background condition and the periods with low hygroscopicity dispersion ($\sigma_{\bar{\kappa}}/\bar{\kappa} < 0.4$) during IOP2 had lower signal to noise ratio due to the low mass loading, but were largely independent of particle size.

Tables

Table S1: Particle diameter classified by the DMA and the corresponding diameters for doubly and triply charged particles. Diameters in the parenthesis represent the measurements (if available) used to correct the contribution of doubly and triply charged particles to the measured activation fractions.

DMA classified singly charged particles, D_p (nm)	Doubly charged particles D_p (nm)	Triply charged particles D_p (nm)
51	75 (75)	94 (94)
75	112 (112)	142 (142)
94	142 (142)	182(171)
112	171 (171)	222 (222)
142	221 (222)	293 (N/A)
171	272 (N/A)	365 (N/A)
222	364 (N/A)	498 (N/A)

Table S2: Criteria used to classify air mass type for different seasons. The threshold values of CN and CO concentrations used to identify background conditions are the mean plus one standard deviation of respective measurements at the background sites T0a and T0t.

Air mass type	Season			
	Wet/Wet 2	Transition 1	Dry	Transition 2
Background	CN<500 cm^{-3} CO<0.14 ppm NO_y<1.5ppbv	CN<900 cm^{-3} CO<0.14 ppm NO_y<1.5ppbv	CN<1500 cm^{-3} NO_y<1.5ppbv	CN<1500 cm^{-3} NO_y<1.5ppbv
Urban Pollution	CN>500 cm^{-3} *$f_{<70} > 0.45$	CN>900 cm^{-3} $f_{<70} > 0.45$	CN>1500 cm^{-3} $f_{<70} > 0.45$	CN>1500 cm^{-3} $f_{<70} > 0.45$
Local biomass burning	CN>500 cm^{-3} $f_{<70} < 0.45$ CO>0.14 ppm	CN>900 cm^{-3} $f_{<70} < 0.45$ CO>0.14 ppm	CN>1500 cm^{-3} $f_{<70} < 0.45$	CN>1500 cm^{-3} $f_{<70} < 0.45$
Site Contamination	BC>1 μg m^{-3} CN>10^4 cm^{-3}	BC>1 μg m^{-3} CN>10^4 cm^{-3}	BC>1 μg m^{-3} CN>10^4 cm^{-3}	BC>1 μg m^{-3} CN>10^4 cm^{-3}

* $f_{<70}$: number fraction of particles with diameters less than 70 nm, derived from SMPS measurement.

Table S3: Classification of air masses for size resolved CCN measurements at 112, 142, and 171 nm, and relevant measurements (CN, CO, SMPS, rBC) averaged to 5-min intervals.

Season	Classification	Percentage of air mass types	
		Size resolved CCN	Relevant measurements
Wet Season 2014	Background	10.2%	17.5%
	Urban Pollution	65.1%	63.7%
	Local Biomass Burning	0.7%	0.6%
	Site Contamination	1.1%	1.3%
	Invalid CCN spectra Fit[#]	12.5%	N/A
	Unclassified[$]	10.5%	17.0%
Transition Season 1	Background	8.9%	11.8%
	Urban Pollution	59.2%	59.1%
	Local Biomass Burning	3.4%	3.6%
	Site Contamination	1.0%	1.2%
	Invalid CCN spectra Fit[#]	4.0%	N/A
	Unclassified[$]	23.6%	24.2%
Dry Season	Background	7.9%	9.7%
	Urban Pollution	14.4%	16.4%
	Local Biomass Burning	68.1%	58.6%
	Site Contamination	1.3%	1.1%
	Invalid CCN spectra Fit[#]	2.9%	N/A
	Unclassified[$]	5.5%	14.3%
Transition Season 2	Background	26.5%	26.9%
	Urban Pollution	11.0%	10.1%
	Local Biomass Burning	50.4%	53.8%
	Site Contamination	1.7%	2.0%
	Invalid CCN spectra Fit[#]	3.3%	N/A
	Unclassified[$]	7.0%	7.3%
Wet Season 2015	Background	8.1%	12.6%
	Urban Pollution	39.6%	41.2%
	Local Biomass Burning	25.6%	24.5%
	Site Contamination	0.8%	0.9%
	Invalid CCN spectra Fit[#]	8.3%	N/A
	Unclassified[$]	17.6%	20.8%
Mar 2014 - Mar 2015	Background	12.4%	16.5%
	Urban Pollution	38.5%	41.2%
	Local Biomass Burning	28.4%	24.7%
	Site Contamination	1.2%	1.3%
	Invalid CCN spectra Fit[#]	6.5%	N/A
	Unclassified[$]	13.0%	16.3%

[#] An invalid fit of the CCN actiation spectrum (Sec. S3.2)

[$] One or more of the measurements (CN, SMPS, CO, rBC) neede to classify air mass is missing or air mass is not classifed as one of the four types using the the criteria described in Table S2.

References

Arnott, W. P., Hamasha, K., Moosmüller, H., Sheridan, P. J., and Ogren, J. A.: Towards Aerosol Light-Absorption Measurements with a 7-Wavelength Aethalometer: Evaluation with a Photoacoustic Instrument and 3-Wavelength Nephelometer, Aerosol Science and Technology, 39, 17-29, 2005.

Collaud Coen, M., Weingartner, E., Apituley, A., Ceburnis, D., Fierz-Schmidhauser, R., Flentje, H., Henzing, J. S., Jennings, S. G., Moerman, M., Petzold, A., Schmid, O., and Baltensperger, U.: Minimizing light absorption measurement artifacts of the Aethalometer: evaluation of five correction algorithms, Atmos. Meas. Tech., 3, 457-474, 2010.

Hansen, A. D. A., Rosen, H., and Novakov, T.: The aethalometer — An instrument for the real-time measurement of optical absorption by aerosol particles, Science of The Total Environment, 36, 191-196, 1984.

Kuwata, M., Zorn, S. R., and Martin, S. T.: Using Elemental Ratios to Predict the Density of Organic Material Composed of Carbon, Hydrogen, and Oxygen, Environmental Science & Technology, 46, 787-794, 2012.

Lance, S., Nenes, A., Medina, J., and Smith, J. N.: Mapping the Operation of the DMT Continuous Flow CCN Counter, Aerosol Science and Technology, 40, 242-254, 2006.

Mei, F., Hayes, P. L., Ortega, A., Taylor, J. W., Allan, J. D., Gilman, J., Kuster, W., de Gouw, J., Jimenez, J. L., and Wang, J.: Droplet activation properties of organic aerosols observed at an urban site during CalNex-LA, Journal of Geophysical Research: Atmospheres, 118, 2903-2917, 2013.

Moteki, N., Kondo, Y., Miyazaki, Y., Takegawa, N., Komazaki, Y., Kurata, G., Shirai, T., Blake, D. R., Miyakawa, T., and Koike, M.: Evolution of mixing state of black carbon particles: Aircraft measurements over the western Pacific in March 2004, Geophys. Res. Lett., 34, L11803 2007.

Petters, M. D. and Kreidenweis, S. M.: A single parameter representation of hygroscopic growth and cloud condensation nucleus activity, Atmos. Chem. Phys., 7, 1961-1971, 2007.

Rizzo, L. V., Correia, A. L., Artaxo, P., Procopio, A. S., and Andreae, M. O.: Spectral dependence of aerosol light absorption over the Amazon Basin, Atmos. Chem. Phys., 11, 8899-8912, 2011.

Roberts, G. C. and Nenes, A.: A Continuous-Flow Streamwise Thermal-Gradient CCN Chamber for Atmospheric Measurements, Aerosol Science and Technology, 39, 206-221, 2005.

Rose, D., Gunthe, S. S., Mikhailov, E., Frank, G. P., Dusek, U., Andreae, M. O., and Poschl, U.: Calibration and measurement uncertainties of a continuous-flow cloud condensation nuclei counter (DMT-CCNC): CCN activation of ammonium sulfate and sodium chloride aerosol particles in theory and experiment, Atmos. Chem. Phys., 8, 1153-1179, 2008.

Schmid, O., Artaxo, P., Arnott, W. P., Chand, D., Gatti, L. V., Frank, G. P., Hoffer, A., Schnaiter, M., and Andreae, M. O.: Spectral light absorption by ambient aerosols influenced by biomass burning in the Amazon Basin. I: Comparison and field calibration of absorption measurement techniques, Atmos. Chem. Phys., 6, 3443-3462, 2006.

Schwarz, J. P., Spackman, J. R., Gao, R. S., Perring, A. E., Cross, E., Onasch, T. B., Ahern, A., Wrobel, W., Davidovits, P., Olfert, J., Dubey, M. K., Mazzoleni, C., and Fahey, D. W.: The Detection Efficiency of the Single Particle Soot Photometer, Aerosol Sci. Technol., 44, 612-628, 2010.

Shilling, J. E., King, S. M., Mochida, M., Worsnop, D. R., and Martin, S. T.: Mass Spectral Evidence That Small Changes in Composition Caused by Oxidative Aging Processes Alter Aerosol CCN Properties, The Journal of Physical Chemistry A, 111, 3358-3368, 2007.

Stephens, M., Turner, N., and Sandberg, J.: Particle identification by laser-induced incandescence in a solid-state laser cavity, Appl. Optics, 42, 3726-3736, 2003.

Virkkula, A., Chi, X., Ding, A., Shen, Y., Nie, W., Qi, X., Zheng, L., Huang, X., Xie, Y., Wang, J., Petaja, T., and Kulmala, M.: On the interpretation of the loading correction of the aethalometer, Atmos. Meas. Tech., 8, 4415-4427, 2015.

Virkkula, A., Mäkelä, T., Hillamo, R., Yli-Tuomi, T., Hirsikko, A., Hämeri, K., and Koponen, I. K.: A Simple Procedure for Correcting Loading Effects of Aethalometer Data, Journal of the Air & Waste Management Association, 57, 1214-1222, 2007.

Weingartner, E., Saathoff, H., Schnaiter, M., Streit, N., Bitnar, B., and Baltensperger, U.: Absorption of light by soot particles: determination of the absorption coefficient by means of aethalometers, Journal of Aerosol Science, 34, 1445-1463, 2003.

Wiedensohler, A.: An approximation of the bipolar charge distribution for particles in the submicron range, J. Aerosol Sci., 19, 387-390, 1988.